Mölsä, Eemeli; Tiitinen, Lauri; Saarakkala, Seppo; Peretti, Luca; Hinkkanen, Marko

Standstill self-commissioning of an induction motor drive

Published in:
ECCE 2020 - IEEE Energy Conversion Congress and Exposition

DOI:
10.1109/ECCE44975.2020.9236035

Published: 11/10/2020

Document Version
Peer-reviewed accepted author manuscript, also known as Final accepted manuscript or Post-print

Please cite the original version:
Mölsä, E., Tiitinen, L., Saarakkala, S., Peretti, L., & Hinkkanen, M. (2020). Standstill self-commissioning of an induction motor drive. In *ECCE 2020 - IEEE Energy Conversion Congress and Exposition* (pp. 3044-3050). Article 9236035 (IEEE Energy Conversion Congress and Exposition). IEEE.
https://doi.org/10.1109/ECCE44975.2020.9236035

Standstill Self-Commissioning of an Induction Motor Drive

Eemeli Mölsä*, Lauri Tiitinen*, Seppo Saarakkala*, Luca Peretti†, and Marko Hinkkanen*
*Aalto University, Department of Electrical Engineering and Automation, Espoo, Finland
†KTH Royal Institute of Technology, Division of Electric Power and Energy Systems, Stockholm, Sweden

***Abstract*—This paper deals with the parameter identification of an induction motor at standstill. A comprehensive identification procedure is analyzed, describing a robust flux-integration method for main-flux saturation characteristics and transient tests for rotor-side parameters. The influence of the main-flux saturation on the transient test results and on the identified rotor-side parameters is studied, and improvements are suggested. The identification procedure is validated by means of experiments using 2.2-kW and 5.6-kW induction motors.**

***Index Terms*—Induction motor drives, parameter identification, saturation characteristics.**

I. Introduction

An induction motor drive is a standard solution in industrial applications. In order to achieve high performance and fast control dynamics, model-based control is often used. Model-based control methods require parameter identification during the drive commissioning. If the Γ model is used, motor parameters can be divided into two groups: 1) stator-side parameters, including the stator resistance and the stator inductance; and 2) rotor-side parameters, including the leakage inductance and the rotor resistance. The stator resistance can be measured simply by means of a DC-test. A standard method to identify the stator inductance is the no-load test [1], but it requires rotating the motor shaft. The rotor-side parameters can be measured by means of the locked-rotor test [1], which, however, is not practical for automatic field-commissioning purposes due to required mechanical arrangements.

The main flux saturates highly as a function of the magnetizing current, already at the nominal operating point. Several standstill methods for identification of the nonlinear stator inductance have been presented, e.g., [2]–[5]. However, these methods are sensitive to the estimation errors of the stator resistance and inverter output voltage, since they are based on integrating the induced stator voltage. In [6], a robust method to identify the stator inductance is proposed. This method requires neither the stator resistance estimate nor the compensation for the inverter nonlinearities.

In [2], [7]–[13], the identification of the rotor-side parameters using transient tests is studied. However, in [8], [10]–[12], the nonlinearity of the stator inductance is omitted. The transient impedance of the induction motor at standstill consists both of the main-flux path and the rotor branch. The transient impedance can be retrieved from the measured voltage and current phasors, if the current amplitude is sufficiently low to stay in the linear magnetic region. The main challenges of this approach are: 1) low voltage amplitudes are difficult to produce and estimate using an inverter due to the dead-time effect; and 2) increasing the voltage is not possible since the saturating inductances would make the current non-sinusoidal, impairing the accuracy of the phasors. In [2], [11], [13], a DC-biased sinusoidal excitation is used to reduce the effect of the inverter nonlinearities. However, the leakage inductance is mistakenly assumed to saturate as a function of the stator current in [2], [13], and the method in [11] does not consider the magnetic saturation of the motor. Furthermore, the cross-saturation effect between the main flux and the rotor leakage flux typically appears in induction motors [14]. This effect may distort standstill identification results if the DC-bias current is used.

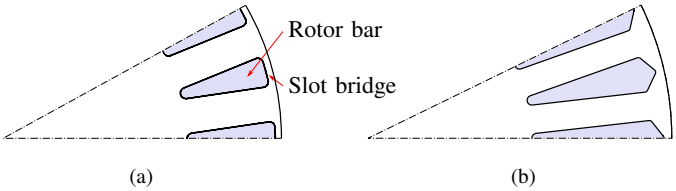

Fig. 1. Rotor cross-sections: (a) 2.2-kW motor; (b) 5.6-kW motor. The rotor slots are closed with thin bridges.

In this paper, we present a standstill identification method for an induction motor. The Γ model with the nonlinear stator inductance is considered. First, the stator inductance is measured using the robust flux-integration method [6]. Then, the rotor-side parameters are identified using the DC-biased single-phase sinusoidal excitation and solving the parameters from the motor model linearized to the actual operating point. The effect of the main-flux saturation on the rotor-side parameter estimates is compensated for. The paper is organized as follows. Section II describes the space-vector model of the saturated induction motor, including the deep-bar effect. Section III presents the identification method, and Section IV shows the experimental results.

II. Motor Model

Fig. 1 shows the rotor cross-sections of two example motors. Both rotors have closed slots and deep bars. The slot bridge in Fig. 1(a) is very thin and almost uniform, and the slot bridge in Fig. 1(b) has a triangular shape. These example geometries result in comparably different saturation characteristics that are to be identified at standstill. Since rotor-side parameter

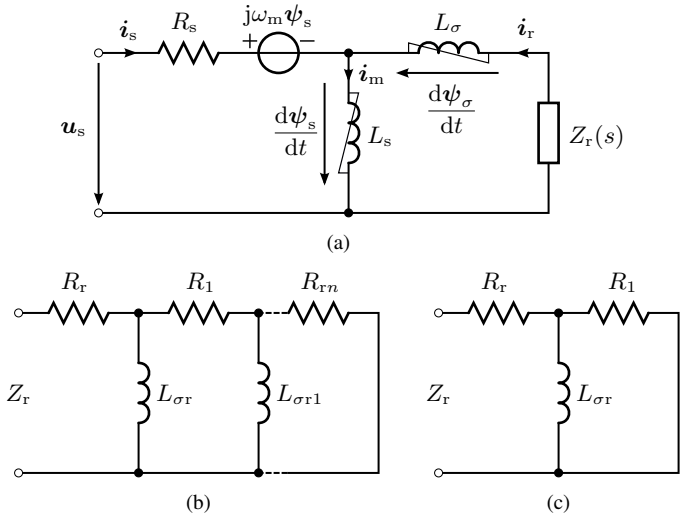

Fig. 2. Motor model in rotor coordinates: (a) Γ model including nonlinear stator inductance L_s, nonlinear slot-bridge inductance L_σ, and rotor-cage impedance Z_r; (b) nth-order rotor-cage impedance; (c) first-order rotor-cage impedance, applied in the proposed method.

identification requires excitation frequencies much higher than rated slip frequencies, the deep-bar effect has to be taken into account.

A. Voltage and Flux Linkage Equations

Fig. 2(a) shows an advanced space-vector Γ model of an induction motor, including models for the magnetic saturation and the deep-bar effect [15]. The model is presented in coordinates rotating at the electrical angular speed ω_m of the rotor, since the rotor-cage impedance is easiest to express in these coordinates. If needed, the model can be easily transformed to other coordinate systems. The voltage equations are

$$\frac{\mathrm{d}\boldsymbol{\psi}_\mathrm{s}}{\mathrm{d}t} = \boldsymbol{u}_\mathrm{s} - R_\mathrm{s}\boldsymbol{i}_\mathrm{s} - \mathrm{j}\omega_\mathrm{m}\boldsymbol{\psi}_\mathrm{s} \tag{1}$$

$$\frac{\mathrm{d}\boldsymbol{\psi}_\sigma}{\mathrm{d}t} = -\boldsymbol{u}_\mathrm{s} + R_\mathrm{s}\boldsymbol{i}_\mathrm{s} + \mathrm{j}\omega_\mathrm{m}\boldsymbol{\psi}_\mathrm{s} - Z_\mathrm{r}(s)\boldsymbol{i}_\mathrm{r} \tag{2}$$

where $\boldsymbol{u}_\mathrm{s}$ is the stator voltage, $\boldsymbol{i}_\mathrm{s}$ is the stator current, $\boldsymbol{i}_\mathrm{r}$ is the rotor current, R_s is the stator resistance, $Z_\mathrm{r}(s)$ is the rotor-cage impedance, and $s = \mathrm{d}/\mathrm{d}t$ is the differential operator. Throughout the paper, the space vectors and other complex quantities are marked with bold.

The stator flux linkage and the rotor leakage flux linkage, respectively, are

$$\boldsymbol{\psi}_\mathrm{s} = L_\mathrm{s}(\boldsymbol{i}_\mathrm{s} + \boldsymbol{i}_\mathrm{r}) \tag{3}$$

$$\boldsymbol{\psi}_\sigma = L_\sigma\boldsymbol{i}_\mathrm{r} \tag{4}$$

where L_s is the saturable stator inductance and L_σ is the saturable leakage inductance. The leakage inductance L_σ models the leakage flux at the rotor slot bridges, while the rotor-cage impedance $Z_\mathrm{r}(s)$ takes the leakage flux through the rotor bars into account. The effect of the stator leakage flux is included in L_s and L_σ [16]. The sum of the stator and rotor currents, $\boldsymbol{i}_\mathrm{m} = \boldsymbol{i}_\mathrm{s} + \boldsymbol{i}_\mathrm{r}$, is referred to as the magnetizing current.

B. Saturation Characteristics

The main-flux path saturates predominantly as a function of the stator flux linkage (or, equivalently, the magnetizing current). Typically, the stator leakage-flux path does not saturate significantly. If the rotor slots are closed, the slot bridges saturate as a function of the rotor leakage flux (or the rotor current).

Induction motors also show cross-saturation effects due to skewed and closed rotor slots [14]. To include these effects, the saturable inductances can be modeled in a general form[1]

$$L_\mathrm{s} = L_\mathrm{s}(\psi_\mathrm{s}, \psi_\sigma) \qquad L_\sigma = L_\sigma(\psi_\mathrm{s}, \psi_\sigma) \tag{5}$$

where $\psi_\mathrm{s} = |\boldsymbol{\psi}_\mathrm{s}|$ and $\psi_\sigma = |\boldsymbol{\psi}_\sigma|$ are the flux-linkage magnitudes. These functions can be represented using look-up tables or explicit functions [4], [14], [15]. If the cross-saturation is omitted, the inductances $L_\mathrm{s} = L_\mathrm{s}(\psi_\mathrm{s})$ and $L_\sigma = L_\sigma(\psi_\sigma)$ can be experimentally characterized by performing the no-load and locked-rotor tests, respectively [15]. The full characterization of the cross-saturation effects requires load tests [14]. If the bias current is used in standstill identification of the rotor-side parameters, the cross-saturation may affect the results.

C. Deep-Bar Effect

Due to the eddy currents in rotor bars, the effective rotor resistance increases and the effective rotor slot inductance decreases as a function of the rotor current frequency [17]. The rotor current frequency equals the slip frequency during normal operation, but the identification of the rotor-side parameters requires injecting higher frequencies to the rotor.

The rotor-cage impedance can be modeled using a ladder circuit shown in Fig. 2(b) [15]. To keep the transfer function $Z_\mathrm{r}(s)$ proper, the circuit must be terminated with a resistor according to the figure. The rotor-cage impedance model can be parametrized by performing a series of locked-rotor tests at different stator frequencies [15].

Since the frequencies of only a few tens of Hertz are needed in standstill identification, the first-order ladder circuit shown in Fig. 2(c) suffices for our purposes. Its transfer function is

$$Z_\mathrm{r}(s) = R_\mathrm{r} + \frac{sL_{\sigma\mathrm{r}}R_{\mathrm{r}1}}{sL_{\sigma\mathrm{r}} + R_{\mathrm{r}1}} \tag{6}$$

As the frequency approaches zero, the resistive impedance approaches R_r and the reactive impedance approaches $sL_{\sigma\mathrm{r}}$. Therefore, the DC rotor resistance R_r and the DC rotor-bar inductance $L_{\sigma\mathrm{r}}$ in (6) can be directly linked to the standard Γ model: its rotor resistance corresponds to R_r and its leakage inductance corresponds to the sum $L_\sigma + L_{\sigma\mathrm{r}}$.

D. Linearized Motor Model

For standstill identification, the model of a saturated motor is linearized, leading to the small-signal model shown in Fig. 3. The motor is assumed to be at standstill, $\omega_\mathrm{m} = 0$. The DC-bias voltage $u_{\mathrm{s}\alpha 0}$ and the small-signal excitation voltage are fed to

[1]Alternatively, the saturation characteristics can be represented in the reciprocal form $L_\mathrm{s} = L_\mathrm{s}(i_\mathrm{m}, i_\mathrm{r})$ and $L_\sigma = L_\sigma(i_\mathrm{m}, i_\mathrm{r})$. We use both forms interchangeably in this paper.

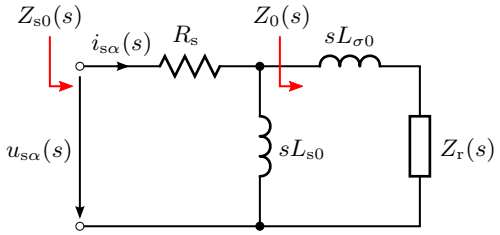

Fig. 3. Small-signal model at standstill, excited to α-axis. The linearized model includes the operating-point stator inductance L_{s0}, the operating-point slot-bridge inductance $L_{\sigma 0}$, and the rotor-cage impedance $Z_r(s)$.

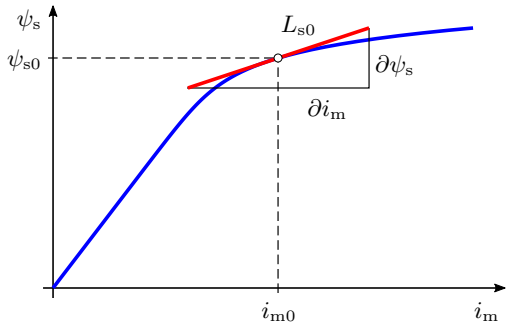

Fig. 4. Incremental inductance L_{s0} at an operating point.

the α-axis direction while $u_{s\beta 0} = 0$. The subscript 0 refers to the operating point. To streamline the notation, we mark the operating-point quantities as $u_{s0} = u_{s\alpha 0}$. Furthermore, we do not separate small-signal and large-signal quantities in the notation, since the meaning should be clear from the context.

The operating point is defined by the DC bias $u_{s0} = R_s i_{s0}$. The operating-point rotor current is $i_{r0} = 0$ and, correspondingly, $\psi_{\sigma 0} = 0$. Consequently, the operating-point stator flux is $\psi_{s0} = L_s(\psi_{s0}, 0) i_{s0}$. The linearization of the model leads to the operating-point incremental inductances

$$L_{s0} = \left(\frac{\partial \psi_s}{\partial i_m}\right)_0 \qquad L_{\sigma 0} = \left(\frac{\partial \psi_{\sigma b}}{\partial i_r}\right)_0 \tag{7}$$

In the single-phase test at standstill, both incremental inductances depend only on ψ_{s0} (or $i_{m0} = i_{s0}$) while $i_{r0} = 0$, as explained above. Fig. 4 shows an example of the stator-flux saturation characteristics and the incremental stator inductance at an operating point. Due to the symmetries of any feasible saturation characteristics about $i_{r0} = 0$, the cross-saturation does not result in additional incremental inductances in the linearized model. However, the incremental leakage inductance $L_{\sigma 0} = L_{\sigma 0}(\psi_{s0}, 0)$ depends on ψ_{s0} due to the cross-saturation. In the Laplace domain, the stator impedance of the small-signal model in Fig. 3 is

$$Z_{s0}(s) = \frac{u_{s\alpha}(s)}{i_{s\alpha}(s)} = R_s + \frac{sL_{s0}Z_0(s)}{sL_{s0} + Z_0(s)} \tag{8}$$

where the impedance of the rotor branch

$$Z_0(s) = sL_{\sigma 0} + Z_r(s) \tag{9}$$

consists of the slot-bridge impedance $sL_{\sigma 0}$ and the rotor-cage impedance $Z_r(s)$.

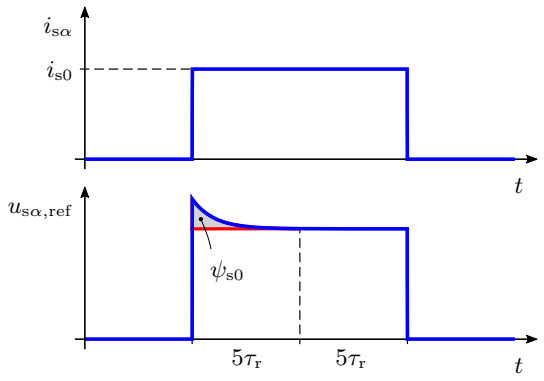

Fig. 5. Principle of the robust flux-integration test. The first integration period of $5\tau_r$ includes the voltage induced from the flux linkage. The second integration period includes only the voltage drop due to the stator resistance and the inverter.

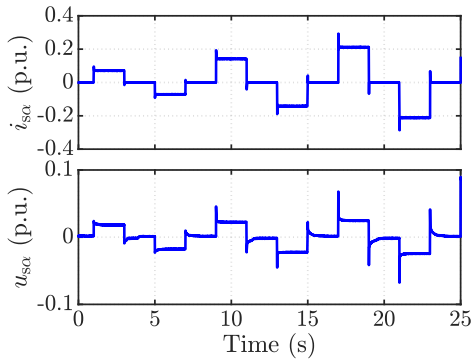

Fig. 6. Flux-integration identification sequence for stator inductance identification. The saturation curve as in Fig. 7 is measured using different current magnitudes.

III. Identification Method

A. Stator Inductance

We apply the robust flux-integration method [6] to measure the stator flux linkage as a function of the magnetizing current. In this method, DC-current steps are supplied to the stator using a current controller.[2] The stator voltage $u_{s\alpha}$ decays to its steady-state value during the regulated current step, as shown in Fig. 5. The stator flux linkage is estimated as

$$\psi_{s0}(i_{s0}) = \int_0^{5\tau_r} u_{s\alpha,ref}\,dt - \int_{5\tau_r}^{10\tau_r} u_{s\alpha,ref}\,dt \tag{10}$$

where i_{s0} is the amplitude of the regulated DC-current, $u_{s\alpha,ref}$ the stator voltage reference, and τ_r is a rough estimate of the rotor time constant. During the first time period, from 0 to $5\tau_r$, the stator voltage $u_{s\alpha}$ includes the induced voltage. At time instant $5\tau_r$, the stator voltage (and stator flux) is assumed to have converged to its steady state values and to consist only of the voltage drop due to the stator resistance and the inverter. Thus, during the second time period from

[2]Since the motor model parameters are not known in advance, the current controller can be tuned using rough parameter estimates. The bandwidth should be low in order to obtain stability.

$5\tau_\mathrm{r}$ to $10\tau_\mathrm{r}$, the stator voltage includes the voltage drop of the stator resistance and the inverter, but not the induced voltage. As both time periods include the same voltage drop term, the latter time period is ruled out without the need to calculate the actual voltage during it, and the voltage reference sent to the modulator $u_{\mathrm{s}\alpha,\mathrm{ref}}$ can be used in (10). The test is repeated using different current magnitudes, as shown in Fig. 6, to identify the saturation curve in Fig. 7. The effect of the current measurement offset is mitigated by repeating the test with both positive and negative currents and by computing the average of the obtained two flux linkage estimates.

For each DC-current value, the chord-slope stator inductance is $L_\mathrm{s} = \psi_{\mathrm{s}0}/i_{\mathrm{s}0}$. The identified inductance values can be stored in a look-up table. Alternatively, an explicit function can be fitted to the identified inductances. In this paper, we use an explicit function [4]

$$L_\mathrm{s}(\psi_\mathrm{s}) = \frac{L_\mathrm{su}}{1 + (\psi_\mathrm{s}/c)^S} \tag{11}$$

where L_su is the unsaturated inductance, and c and S are positive constants. The corresponding operating-point incremental inductance is

$$L_{\mathrm{s}0}(\psi_\mathrm{s}) = \frac{L_\mathrm{su}}{1 + (1+S)(\psi_\mathrm{s}/c)^S} \tag{12}$$

which is needed in identification of the rotor-side parameters.

B. Rotor-Cage Impedance

The excitation signal for identifying the rotor-side parameters has to include adequately high frequencies, since frequencies lower than the inverse rotor time constant access mainly the main-flux path. To avoid distortions due to the deep-bar effect, we first identify the three parameters of the rotor-cage impedance model (6). A DC-biased sinusoidal voltage is used to maintain the current sign unchanged, which decreases the effect of inverter nonlinearities. The voltage excitation signal is

$$u_{\mathrm{s}\alpha}(t) = u_{\mathrm{s}0} + u_1 \sin(\omega t) \tag{13}$$

where $u_{\mathrm{s}0}$ is the bias voltage, u_1 the amplitude, and ω the angular frequency of the signal. The bias voltage $u_{\mathrm{s}0}$ corresponding to the nominal magnetizing current is a trivial choice. The amplitude u_1 should be adequately low to stay in the small-signal area and to be able to use the model (8).

The stator impedance is calculated from the measurements as

$$\boldsymbol{Z}_{\mathrm{s}0}(\mathrm{j}\omega) = \frac{\boldsymbol{u}_{\mathrm{s}\alpha}(\omega)}{\boldsymbol{i}_{\mathrm{s}\alpha}(\omega)} \tag{14}$$

where $\boldsymbol{u}_{\mathrm{s}\alpha}$ and $\boldsymbol{i}_{\mathrm{s}\alpha}$ are the phasors calculated from the voltage estimate and the measured phase currents, respectively, using the discrete Fourier transform. The impedance of the rotor-branch solved from (8) and (9) is

$$\boldsymbol{Z}_0(\mathrm{j}\omega) = \frac{\mathrm{j}\omega L_{\mathrm{s}0}[\boldsymbol{Z}_{\mathrm{s}0}(\mathrm{j}\omega) - R_\mathrm{s}]}{\mathrm{j}\omega L_{\mathrm{s}0} + R_\mathrm{s} - \boldsymbol{Z}_{\mathrm{s}0}(\mathrm{j}\omega)} \tag{15}$$

Therefore, as the stator impedance $\boldsymbol{Z}_{\mathrm{s}0}(\mathrm{j}\omega)$ is known after the measurement, and the incremental stator inductance $L_{\mathrm{s}0}$ in the operating point is known after the robust flux-integration test, the rotor-branch impedance can be calculated from (15) for each ω and $u_{\mathrm{s}0}$. The incremental inductance $L_{\mathrm{s}0} = L_{\mathrm{s}0}(\psi_{\mathrm{s}0})$ needed in (15) can be computed using (12) for each bias flux $\psi_{\mathrm{s}0} = L_\mathrm{s}(\psi_{\mathrm{s}0})i_{\mathrm{s}0}$. It is worth noticing that the DC-bias current may saturate the stator inductance, but this effect is taken into account in (15) using the results from the flux-integration method, as explained above.

According to (9), the resistive rotor-cage impedance equals the resistive rotor-branch impedance

$$\mathrm{Re}\{\boldsymbol{Z}_\mathrm{r}(\mathrm{j}\omega)\} = \mathrm{Re}\{\boldsymbol{Z}_0(\mathrm{j}\omega)\} \tag{16}$$

and does not depend on the $L_{\sigma 0}$. Therefore, the parameters $L_{\sigma\mathrm{r}}$, R_r, and $R_{\mathrm{r}1}$ of the rotor-cage impedance model (6) can be estimated by means of fitting the resistive part $\mathrm{Re}\{\boldsymbol{Z}_\mathrm{r}(\mathrm{j}\omega)\}$ of the model to the measured values $\mathrm{Re}\{\boldsymbol{Z}_0(\mathrm{j}\omega)\}$. A minimum of three different excitation frequencies are needed to estimate the three parameters.

C. Leakage Inductance

Finally, according to (9), the incremental leakage inductance can be solved from (14) as

$$L_{\sigma 0} = \frac{\mathrm{Im}\{\boldsymbol{Z}_0(\mathrm{j}\omega) - \boldsymbol{Z}_\mathrm{r}(\mathrm{j}\omega)\}}{\omega} \tag{17}$$

If the stator impedance in (14) is measured at different bias voltages (corresponding to the magnetizing currents), the effect of the cross saturation on $L_{\sigma 0}$ can be captured.

IV. Experimental Results

A. Experimental System

The method is validated by means of experiments using 2.2-kW and 5.6-kW induction motors. Both motors are of the closed rotor-slot type and their rotor-slot structures are shown in Fig. 1. A three-phase inverter, controlled by a dSPACE MicroLabBox system, is used to supply the motors. The stator current and the DC-link voltage are measured at the sampling frequency of 4 kHz. The stator voltage is estimated from the inverter switch duty ratios and the measured DC-link voltage. The effect of the computational and PWM delays on the realized voltage is compensated for, while the inverter nonlinearities are left uncompensated. The motor is assumed to stay at standstill during the tests. Some mechanical fluctuation of the rotor angle might appear due to the magnetic remanence, when the stator current sign changes, but this phenomenon is not considered.

B. Benchmark Results

The benchmark characteristics of the motors were measured using the sinusoidal voltage supply according to the procedure described in [15]. A series of no-load tests is performed using different stator current (or magnetizing current) levels in order to obtain the stator-flux saturation characteristics. The rotor-cage impedance is measured by completing a series of locked-rotor tests at different stator frequencies. Moreover, the saturation characteristics of the rotor slot-bridge are measured

TABLE I
PARAMETERS OF THE FOUR-POLE INDUCTION MOTORS

	2.2-kW motor	5.6-kW motor
Rated values		
Voltage (rms, line-line)	400 V	460 V
Current (rms)	5 A	9.5 A
Frequency	50 Hz	60 Hz
Speed	1475 r/min	1770 r/min
Stator resistance R_s	3.5 Ω	0.9 Ω
Stator inductance		
Unsaturated inductance L_su	340 mH	174 mH
Coefficient c	1.12 $(\mathrm{Vs})^{-1}$	1.45 $(\mathrm{Vs})^{-1}$
Coefficient S	11.2	7.6
Incremental leakage inductance $L_{\sigma 0}$	26 mH	16 mH
Rotor-cage impedance		
DC-inductance $L_{\sigma \mathrm{r}}$	4 mH	3 mH
DC-resistance R_r	1.7 Ω	0.6 Ω
Resistance $R_{\mathrm{r}1}$	2.7 Ω	1.6 Ω

by completing another series of locked-rotor tests, but keeping the stator frequency constant and varying the stator current amplitude. Fig. 7 shows the results of the no-load tests for both motors. Figs. 8 and 9 show the measured rotor-cage impedance and the rotor slot-bridge saturation characteristics, respectively.

C. Proposed Standstill Identification

1) Stator Inductance: The nonlinear stator inductance is measured using the robust flux-integration test as described in Section III-A. Fig. 7 shows the identified stator flux linkage values together with the fitted saturation model (11), where the no-load test results are shown as a reference. The measured data points and the fitted model are close to the benchmark no-load test results. The parameters of the fitted saturation model are given in Table I.

2) Rotor-Cage Impedance: The rotor-cage impedance is identified using the single-phase test described in Section III-B. The amplitude of the single-phase excitation voltage could be chosen to be proportional to the excitation frequency. However, in this paper, we use the constant voltage $u_1 = 0.015$ p.u. in all tests.

Fig. 8 shows the resistive part of the rotor-branch impedance (15) calculated from the measured stator impedance. The solid curve represents the ladder-circuit model (6) fitted to the impedance values. It can be seen that the model fits very well with the data. The DC offset in the calculated impedances depends strongly on the stator resistance estimate, cf. (15). The locked-rotor test results show similar sensitivity. Since the current and DC-bus voltage measurement channels of the inverter were not calibrated, some offset difference between the single-phase and locked-rotor tests could be expected, as also visible in Fig. 8(b). However, perfectly accurate parameters are not of interest for control purposes, but parameters should match with imperfectly calibrated measurement channels of the inverter.

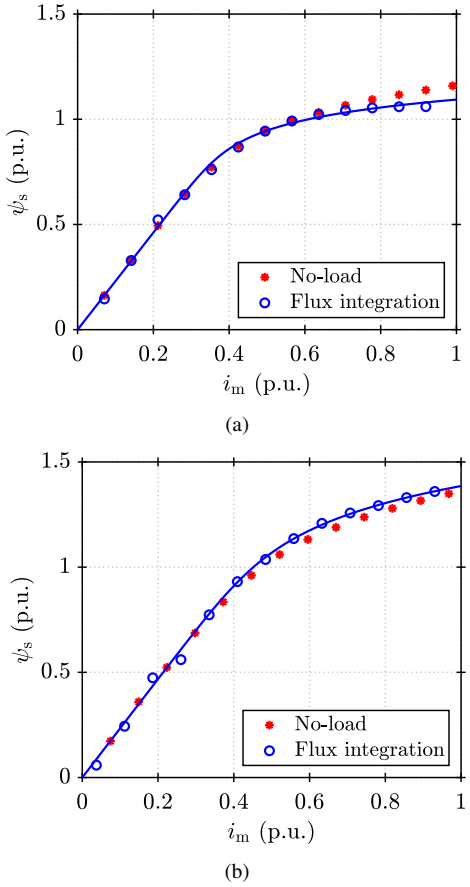

Fig. 7. Stator-flux saturation characteristics: (a) 2.2-kW motor; (b) 5.6-kW motor. The red markers are the results of the no-load tests and the blue markers are the results of the robust flux-integration test. The solid line corresponds to the model (11) fitted to the robust flux-integration test. The nominal magnetizing current of the 2.2-kW and 5.6-kW motors are 0.5 p.u. and 0.4 p.u., respectively.

Table I gives the fitted parameters of the cage-impedance model. The DC rotor resistance R_r and the DC inductance $L_{\sigma \mathrm{r}}$ can be directly used to parametrize the standard Γ model for control purposes (while the parameter $R_{\mathrm{r}1}$ is not needed). If high accuracy at large slip frequencies is needed, the first-order ladder-circuit together with all three parameters can be used in control.

3) Leakage Inductance: Fig. 9 shows the identified incremental leakage inductance $L_{\sigma 0}$ calculated from the measured stator impedance using (17), as a function of the bias current. The results from the locked-rotor tests are also shown, corresponding to the chord-slope inductance L_σ as a function of the rotor current.

In the case of the 2.2-kW motor, the results from the locked-rotor test in Fig. 9(a) show that the leakage inductance L_σ is approximately constant. Overall, the results of the single-phase test match very well with the results from the locked-rotor tests. In the single-phase test, the elevation of the identified leakage inductance at high bias currents originates from the inaccuracies in the identified incremental stator inductance $L_{\mathrm{s}0}$, visible in Fig. 7(a). It is also to be noted that if the stator

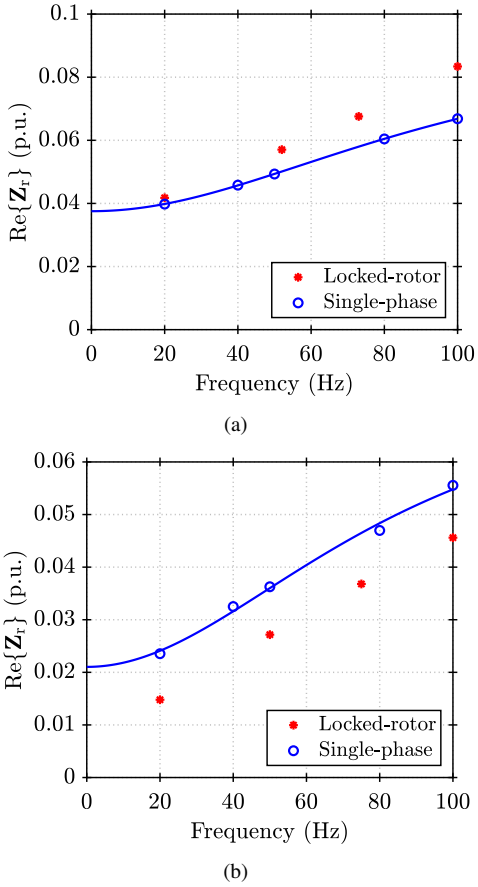

Fig. 8. Resistive part of the rotor-branch impedance: (a) 2.2-kW motor; (b) 5.6-kW motor. The red markers are the benchmark values, obtained by means of the locked-rotor tests with the stator current magnitude $i_{\mathrm{s}0} = 0.33$ p.u. The solid lines correspond to the model (6) fitted to the single-phase test (bias corresponds to the nominal magnetizing current).

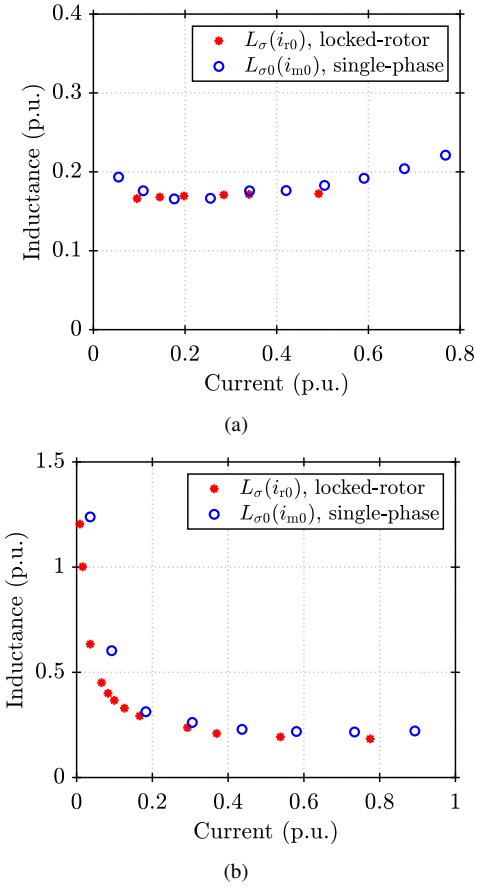

Fig. 9. Identified leakage inductance: (a) 2.2-kW motor; (b) 5.6-kW motor. The blue markers show the identified values (17). The red markers are the benchmark values obtained from the locked-rotor tests.

inductance saturation were omitted, the identified leakage inductance would become too low at large bias currents.

In the case of the 5.6-kW motor, the results from the locked-rotor test in Fig. 9(b) show that the leakage inductance L_σ (i.e., rotor slot bridges) saturate highly as a function of the rotor current $i_{\mathrm{r}0}$. Furthermore, the saturation characteristics $L_{\sigma 0}(i_{\mathrm{m}0})$ measured with the single-phase test are very similar to the characteristics $L_\sigma(i_{\mathrm{r}0})$. This result indicates strong cross-saturation of the 5.6-kW motor.

The identified incremental inductance values at the nominal magnetizing current are given in Table I. The difference between the incremental and chord-slope inductances is expected to be minor in deep saturation. For control purposes, the total leakage inductance may be approximated as a sum $L_{\sigma 0} + L_{\sigma \mathrm{r}}$ of the incremental leakage inductance corresponding the nominal magnetizing current and the rotor-cage DC-inductance.

V. Conclusions

The paper presents a comprehensive procedure to identify the induction motor parameters at standstill. For estimating the saturable stator inductance, we use the robust flux-integration method. The rotor-side parameters are identified by means of the transient test, using the DC-biased sinusoidal excitation. The nonlinear stator inductance and the deep-bar effect are taken into account in the proposed identification method.

References

[1] P. L. Alger, *The Nature of Induction Machines*. New York: Gordon and Breach, 1965.

[2] L. Peretti and M. Zigliotto, "Automatic procedure for induction motor parameter estimation at standstill," *IET Electr. Power Appl.*, vol. 6, no. 4, pp. 214–224, Apr. 2012.

[3] C. Sukhapap and S. Sangwongwanich, "Auto tuning of parameters and magnetization curve of an induction motor at standstill," in *Proc. IEEE ICIT*, vol. 1, Dec. 2002, pp. 101–106.

[4] N. R. Klaes, "Parameter identification of an induction machine with regard to dependencies on saturation," *IEEE Trans. Ind. Appl.*, vol. 29, no. 6, pp. 1135–1140, Nov./Dec. 1993.

[5] S. Khamehchi, E. Mölsä, and M. Hinkkanen, "Comparison of standstill parameter identification methods for induction motors," in *Proc. IEEE SLED*, Sep. 2018, pp. 156–161.

[6] F. Erturk and B. Akin, "A robust method for induction motor magnetizing curve identification at standstill," *IEEE Access*, vol. 7, pp. 55 422–55 431, 2019.

[7] R. J. Kerkman, J. D. Thunes, T. M. Rowan, and D. W. Schlegel, "A frequency-based determination of transient inductance and rotor resistance for field commissioning purposes," *IEEE Trans. Ind. Appl.*, vol. 32, no. 3, pp. 577–584, May/Jun. 1996.

[8] S. R. Shaw and S. B. Leeb, "Identification of induction motor parameters from transient stator current measurements," *IEEE Trans. Ind. Electron.*, vol. 46, no. 1, pp. 139–149, Feb 1999.

[9] A. Gastli, "Identification of induction motor equivalent circuit parameters using the single-phase test," *IEEE Trans. Energy Convers.*, vol. 14, no. 1, pp. 51–56, Mar. 1999.

[10] S. Lee, A. Yoo, H. Lee, Y. Yoon, and B. Han, "Identification of induction motor parameters at standstill based on integral calculation," *IEEE Trans. Ind. Appl.*, vol. 53, no. 3, pp. 2130–2139, May 2017.

[11] G. Shen, K. Wang, W. Yao, K. Lee, and Z. Lu, "Dc biased stimulation method for induction motor parameters identification at standstill without inverter nonlinearity compensation," in *Proc. IEEE ECCE*, Sep. 2013, pp. 5123–5130.

[12] Hao Ge, Jing Guo, B. Bilgin, Jin Ye, V. Loukanov, and A. Emadi, "A reduced-order model based induction machine self-commissioning method," in *Proc. IEEE ITEC*, Jun. 2015, pp. 1–8.

[13] M. Carraro and M. Zigliotto, "Automatic parameter identification of inverter-fed induction motors at standstill," *IEEE Trans. Ind. Electron.*, vol. 61, no. 9, pp. 4605–4613, Sep. 2014.

[14] T. Tuovinen, M. Hinkkanen, and J. Luomi, "Modeling of saturation due to main and leakage flux interaction in induction machines," *IEEE Trans. Ind. Appl.*, vol. 46, no. 3, pp. 937–945, May/Jun. 2010.

[15] E. Mölsä, S. E. Saarakkala, M. Hinkkanen, A. Arkkio, and M. Routimo, "A dynamic model for saturated induction machines with closed rotor slots and deep bars," *IEEE Trans. Energy Convers.*, vol. 35, no. 1, pp. 157–165, Mar. 2020.

[16] G. R. Slemon, "Modelling of induction machines for electric drives," *IEEE Trans. Ind. Appl.*, vol. 25, no. 6, pp. 1126–1131, Nov./Dec. 1989.

[17] S. Williamson and M. C. Begg, "Calculation of the bar resistance and leakage reactance of cage rotors with closed slots," *IEE Proc. B, Electr. Power Appl.*, vol. 132, no. 3, pp. 125–132, May 1985.